

Two-dimensional intrinsic ferrovalley GdI₂ with large valley polarizationHai-Xia Cheng^{1,2}, Jun Zhou^{3,*}, Wei Ji², Yan-Ning Zhang^{1,*} and Yuan-Ping Feng^{3,4,*}¹*Institute of Fundamental and Frontier Sciences, University of Electronic Science and Technology of China, Chengdu 610054, China*²*Department of Physics, Renmin University of China, Beijing 100872, China*³*Department of Physics, National University of Singapore, Singapore 117551*⁴*Center for Advanced 2D Materials, National University of Singapore, Singapore 117546*

(Received 29 December 2020; accepted 10 February 2021; published 10 March 2021)

Manipulation of the valley degree of freedom provides a novel paradigm in quantum information technology. In this work, through first principles calculations, we demonstrate that monolayer GdI₂ is a promising candidate material for valleytronic applications. Monolayer GdI₂ can be easily exfoliated from bulk, and it is spontaneously valley polarized with a giant splitting of 149 meV due to its intrinsic ferromagnetism and large spin orbital coupling. The anomalous valley Hall effect could be realized in monolayer GdI₂ by an appropriate external electric field. Furthermore, the valley polarization feature is stable against the biaxial in-plane strain. Our findings provide an extraordinary and potential material platform for experimental studies and practical applications in the emergent field of valleytronics.

DOI: [10.1103/PhysRevB.103.125121](https://doi.org/10.1103/PhysRevB.103.125121)**I. INTRODUCTION**

Valley, a new degree of freedom in addition to charge and spin of carriers, is characterized by a local energy extreme in the conduction band or valence band. An ideal valley material has two or more degenerate but inequivalent valley states at the inequivalent k points in the momentum space [1,2]. The valley degree of freedom can be encoded and manipulated as information carriers in the next-generation information technology (e.g., valleytronics) [2–4], since the large separation between the two inequivalent valleys in the momentum space will greatly suppress the intervalley scattering induced by deformation and long wavelength phonon. The basic and significant principle to realize applications of valleytronics is that carriers in different valleys must be selectively produced or manipulated. Hence, lifting the energy degeneracy between the two valleys with large valley splitting is necessary to selectively access valley states as well as to minimize the effect of thermal noise in the device.

Two-dimensional (2D) transition metal dichalcogenides (TMDs) have attracted extensive attention as potential 2D valley materials. Their broken spatial inversion symmetry leads to two degenerate but inequivalent valley states at the K and K' points of hexagonal Brillouin zone [5–7], which are named as K valley materials. However, most of the known 2D TMD valley materials have no spontaneous valley splitting due to their time reversal symmetry. Extrinsic approaches have been proposed to induce a valley polarization in TMDs, including employing an external magnetic field [8,9], optical pumping [6], doping of magnetic elements [10,11] and magnetic proximity effects [12–16]. However, these extrinsic methods are

not ideal for practical applications. For example, the efficiency of valley polarization generated by the external magnetic field is very low ($0.1 \sim 0.2$ meV/T); optical pumping as a dynamic process is difficult to control; magnetic transition metal dopants have a tendency to form clusters on the surface of TMD films and increase the scattering during transport process; the magnetic substrates for proximity effects enlarge the device size and may impact the device performance. Recently, ferrovalley [17] materials were proposed, which are a new class of materials with intrinsic spontaneous valley polarization introduced by their intrinsic ferromagnetism, offering an opportunity to address these challenges of the extrinsic valley polarization materials. However, only a few ferrovalley materials have been identified hitherto, including 2H-VSe₂ [17], VAgP₂Se₆ [18], LaBr₂ [19,20], NbX₂ ($X = S, Se$) [21], Nb₃I₈ [22], TiVI₆ [23], and so on. Unfortunately, the low experimental feasibility, small intrinsic valley splitting gap, and low Curie temperature hamper the practical applications of these 2D ferrovalley materials. Thus, high Curie temperature ferrovalley materials with large valley polarization are urgently needed for the next-generation electronics.

Monolayer (ML) GdI₂ is isostructural to 2H-MoS₂, and the similar broken inversion symmetry and K valleys as in 2H-MoS₂ can be expected in ML GdI₂. Furthermore, recent first principles calculations have predicted that the ML GdI₂ is a ferromagnetic semiconductor with a high Curie temperature of 241 K [24], which spontaneously breaks the time reversal symmetry. Last but not least, Gd is a heavy rare earth element with f electrons. Its strong spin-orbital coupling (SOC) is expected to give rise to a large splitting between two valleys. In light of all these properties, ML GdI₂ is likely to be a ferrovalley material with a large spontaneous valley splitting, and a ferrovalley transition temperature close to room temperature. In this work, via first principles simulations, we first show that ML GdI₂ can be easily exfoliated from parent

*Authors to whom correspondence should be addressed: phyzjun@nus.edu.sg; yanningz@uestc.edu.cn; phyfyp@nus.edu.sg

layered bulk crystal. Then, a large spontaneous valley splitting is revealed in ML GdI₂ by its band structure including the SOC effect. We also confirm the anomalous valley Hall effect can be realized in this material. And the valley polarization can be further enhanced by applying biaxial tensile strains. These results make ML GdI₂ an appealing intrinsic ferrovalley material for valleytronics.

II. COMPUTATIONAL DETAILS

The first principles calculations are performed using the projector augmented-wave [25,26] method as implemented in the Vienna ab initio package [27,28]. The Perdew-Burke-Ernzerhof (PBE) [29] type generalized gradient approximation (GGA) [30] is used to treat the exchange-correlation interaction between electrons. The van der Waals (vdW) correction is considered for bulk GdI₂ using the density functional theory (DFT)-D2 method [31]. Throughout this work, spin polarization is included except in spin orbital coupling calculations. Energy cutoff for the plane wave basis is 500 eV. The Brillouin zone is sampled using a converged Γ -centered $9 \times 9 \times 1$ k mesh for structural relaxation and $17 \times 17 \times 1$ for electronic analyses. Both atomic positions and lattice constants are relaxed until the forces and energies are converged to 0.01 eV/Å and 10^{-6} eV/atom, respectively. For ML GdI₂, a vacuum space of about 20 Å is applied along the c direction to avoid the interaction between adjacent layers. The GGA+U method [32] is adopted to push the unoccupied Gd-4*f* orbitals away from Fermi level, and the Hubbard U parameter is set to 4.6 eV [33]. The HSE06 hybrid functional is employed in the calculations of band structures to check the reliability of the electronic structure by the PBE+U method. SOC [34] is incorporated for self-consistent energy and band structure calculations. Phonon dispersion spectrum of ML GdI₂ is obtained by the PHONOPY code [35] based on the density of functional perturbation theory [36] using a $3 \times 3 \times 1$ supercell. *Ab initio* molecular dynamic (AIMD) [37] simulation is carried out in a canonical ensemble [38] based on the algorithm of Nosé [39] at a temperature of 300 K with a $3 \times 3 \times 1$ supercell. The Berry curvature and anomalous Hall conductivity of ML GdI₂ are calculated by means of maximally localized Wannier functions implemented in the WANNIER90 package [40].

III. RESULTS AND DISCUSSIONS

A. Mechanical exfoliation and Structural stability of ML GdI₂

Bulk GdI₂, which is ferromagnetic with a large saturation magnetic moment of about $7.33 \mu_B$ per Gd atom near room temperature (its Curie temperature is about 290 ~ 340 K) [41–43]. It has a vdW layered 2H-MoS₂ type structure [44], in which the I-Gd-I sandwich layers are stacked together along the c axis as shown in Fig. S1(a) of the Supplemental Material (SM) [45]. To estimate the possible mechanical exfoliation of ML GdI₂, exfoliation energy is calculated using a four-layer slab model with the increasing separation distance between the top layer and next layer (details are presented in Part I of the SM [45]). As shown in Fig. 1(a), the energy increases and eventually converges to 0.24 J/m² which is taken as the

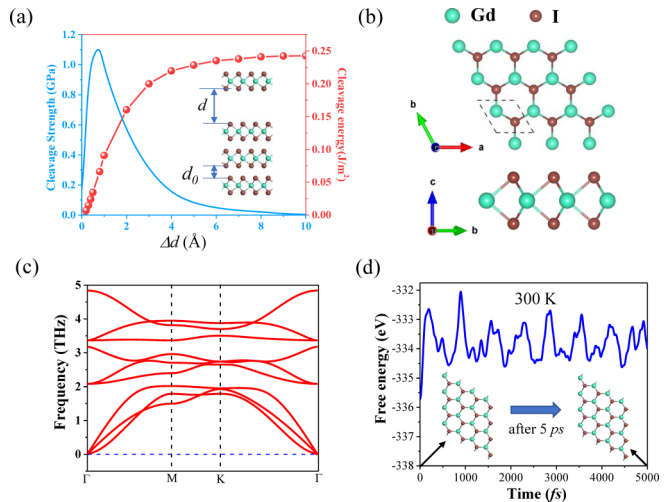


FIG. 1. Geometry and stability of ML GdI₂. (a) Simulated exfoliation process (inset structure). $\Delta d = d - d_0$ refers to the changes of interlayer space between top and adjacent layers. d_0 is the equilibrium vdW gap in bulk. (b) Top and side views of ML GdI₂. The rhombus in dashed line denotes the unit cell. (c) Phonon dispersion spectrum and (d) variation of free energy during the 5 ps *ab initio* molecular dynamics simulation of ML GdI₂. Insets in (d) show the initial and final structures of ML GdI₂ after 5 ps at 300 K.

exfoliation energy. For comparison, the exfoliation energy of graphene is also calculated to be 0.33 J/m² with the same method (Fig. S2 of the SM [45]), which is in good agreement with the experimentally measured value of 0.36 J/m² [46]. The smaller exfoliation energy of GdI₂ than graphene's indicates it is feasible to exfoliate ML GdI₂ experimentally. The calculated Young's modulus of ML GdI₂ is 32.62 N/m, which is about 0.1 times smaller than that of graphene [47], suggesting that GdI₂ possesses better mechanical flexibility. Based on the elastic theory [48], ML GdI₂ is able to withstand its own weight and maintain a free-standing planar structure during the exfoliation process (see Part I of the SM [45]).

The crystal structure of ML GdI₂ is shown in Fig. 1(b). The unit cell of ML GdI₂ contains one Gd atomic layer, sandwiched by two I atomic layers. The central Gd atoms are trigonal prismatic coordinated with six I atoms. The relaxed equilibrium lattice constants of ML GdI₂ are $a = b = 4.099$ Å [see Fig. S1(b) in the SM [45]], which are slightly smaller than their bulk values by DFT calculation ($a = b = 4.104$ Å). The thermal dynamic stability of ML GdI₂ is estimated by the phonon dispersion spectrum and AIMD calculations. The absence of imaginary modes in the phonon dispersion spectrum confirms that ML GdI₂ is dynamically stable [Fig. 1(c)]. The free energies of ML GdI₂ during 5 ps with a time step of 1 fs at 300 K by AIMD simulations are shown in Fig. 1(d). The insets are snapshots of the geometry at 0 ps and 5 ps, respectively. The small fluctuations of energy and integrity of original configuration with time evolution demonstrate good thermal stability of ML GdI₂. The phase diagram including ML GdI₂ and other Gd-I compounds [49] is also plotted (see Fig. S3 in the SM [45]). ML GdI₂ is on the hull curve, indicating its thermodynamic stability.

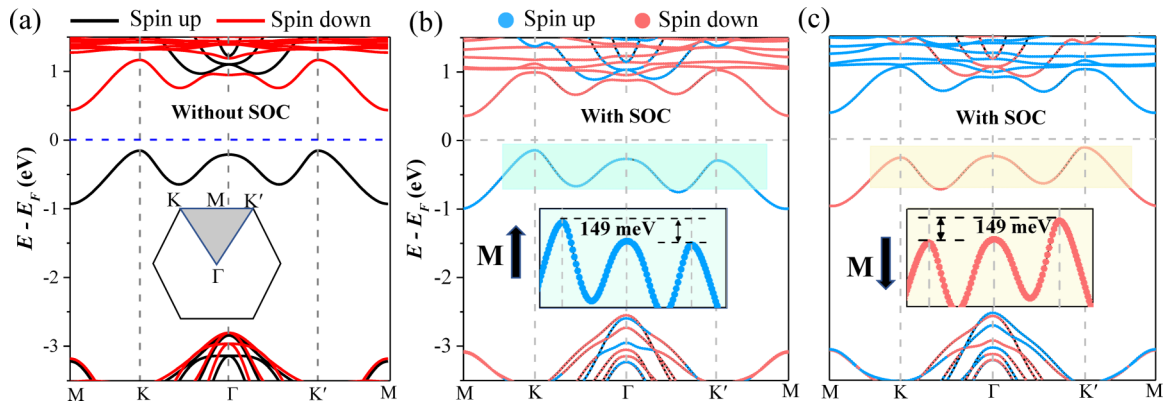


FIG. 2. The band structure of ML-GdI₂ (a) without SOC; (b) and (c) with SOC for magnetic moment of Gd along the positive and negative z direction (out of plane), respectively. Spin projections along the out of plane direction are indicated by red (positive direction, spin-up) and blue (negative direction, spin-down) circles for GdI₂ orbitals in (b) and (c). The dashed horizontal lines refer to the Fermi level. 2D Brillouin zone of GdI₂ is shown in the inset of (a).

B. Spin and valley polarization of ML GdI₂

In GdI₂, two electrons are transferred from one Gd atom to the six neighboring I atoms, yielding Gd²⁺ and I¹⁻, and the electronic configuration of Gd is $4f^7 5d^1$. The half-filled $4f$ shell and $5d$ shell will lead to the theoretical magnetic moment of about $8 \mu_B/\text{Gd}$. The DFT calculated saturation magnetic moment of Gd is $7.446 \mu_B$ in ML GdI₂, which is in good agreement with the experimental value ($7.335 \mu_B/\text{Gd}$) for bulk [43]. To study the ground magnetic configuration of ML GdI₂, the energies of the ferromagnetic and antiferromagnetic states with a $2 \times 2 \times 1$ supercell are compared. The ferromagnetic state is found to be energetically lower than that of the antiferromagnetic state by $134 \text{ meV}/\text{Gd}$ as shown in Fig. S4 of the SM [45], suggesting a strong ferromagnetic coupling in monolayer GdI₂. The result is consistent with the prediction of other theoretical calculation ($139 \text{ meV}/\text{Gd}$) [24].

Figure 2(a) shows the spin-polarized band structure of the ML GdI₂. It can be seen that the spin splitting leads to an indirect band gap of 0.589 eV with valence band maximum (VBM) at the K and conduction band minimum (CBM) at the M high symmetry points. Around the Fermi level, the fully spin-polarized valence band and conduction band in opposite spin channels make ML GdI₂ a bipolar magnetic semiconductor [50–54], in which 100% spin polarized carriers can be readily obtained by manipulating Fermi level (more details are shown in Part III and Fig. S5 of the SM [45]). The band structure calculated by HSE06 functional has a larger band gap (1.08 eV) but the profile of bands has negligible difference compared with the one calculated by PBE+U functional (see Fig. S6 of the SM [45]). For the sake of computational cost, PBE+U is used for all the calculations of ML GdI₂ unless otherwise stated. More importantly, a pair of degenerate energy extremes localize at the K and K' high-symmetry points of 2D Brillouin zone in the valence band, making the ML GdI₂ a valley material.

As shown in Fig. 2(b), the SOC lifts the degeneracy between the K and K' valley states (the energy of K valley state is higher than K' valley's) in the valence band, leading to a spontaneous valley polarization with a large valley splitting of 149 meV in ML GdI₂, which is equivalent to applying

a huge external magnetic field of around $745\text{--}1490 \text{ T}$. And the valley splitting of ML GdI₂ is much larger than that in other reported ferrovalley materials, e.g., 2H-VSe_2 (89 meV) [17], VAgP_2Se_6 (15 meV) [18], LaBr_2 (33 meV) [20], Nb_3I_8 (107 meV) [22], and TiVI_6 (22 meV) [23]. To be a useful valley material, breaking the degeneracy between the K and K' states is critically important, and the valley splitting must be large enough to overcome the thermal noise, e.g., a 100 meV valley splitting is estimated to be necessary for room temperature operation [55,56]. Therefore, such a large valley splitting gap in ML GdI₂ will lead to nonvolatile valley polarization and readily manipulated valley states at room temperature for logic applications. Furthermore, there is no trivial band inside the transport energy window from -1 to 0 eV . The valley polarization of ML GdI₂ is also tunable by an external magnetic field. As shown in Fig. 2(c), the spin and valley polarization can be flipped simultaneously by reversing the magnetization of Gd atoms, namely, K/K' valley states in valence band now occupy the spin-down channel and the K valley state has a lower energy than K' valley. In this situation, the carriers come from K' valley state in the spin-down channel when the Fermi level is pushed down to the energy range between K' and K valleys. This provides an efficient way to tune the valley properties of the ML GdI₂ by manipulating its direction of magnetization. Overall, combined with its reported high Curie temperature [24], ML GdI₂ is an ideal ferrovalley material for the practical applications such as valley filter, valley valves, and other valleytronic devices.

The underlying physic for the spontaneous valley polarization in ML GdI₂ is attributed to the joint effects of the intrinsic magnetic exchange field and strong spin orbital coupling. As shown in Fig. 2(a), with spin polarization but excluding SOC, the spin-up and spin-down states are completely split by the magnetic exchange interaction, but the energetic degeneracy between K and K' are preserved. The orbital projected band structure and density of states of Gd atom as well as partial charge density of CBM and VBM are plotted to investigate their orbital contribution. As shown in Figs. S7 and S8 of the SM [45], the valley states at the K and K' are mainly contributed by the occupied $d_{x^2-y^2}$ and d_{xy} orbitals of Gd. The Gd- d_{z^2} mostly distributes around the Γ point. Also, the $d_{x^2-y^2}$

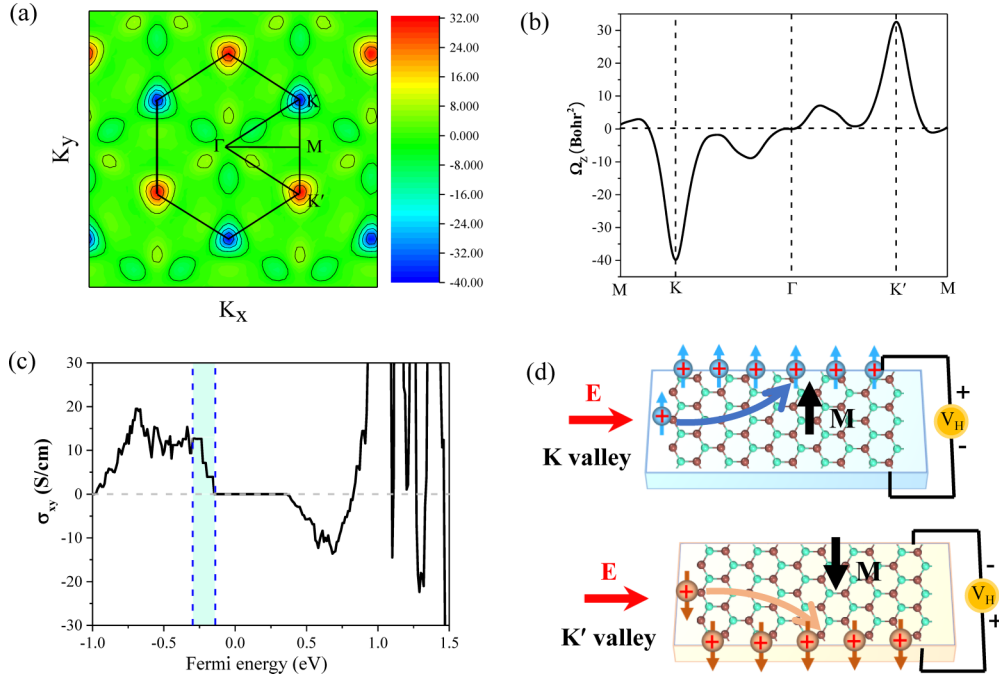


FIG. 3. Berry curvature of ML GdI $_2$ in (a) a contour map in the 2D Brillouin zone and (b) along the high symmetry points. (c) Calculated anomalous Hall conductivity σ_{xy} as a function of Fermi energy for ML GdI $_2$. The two vertical dashed lines denote the two valley extrema. (d) Schematic diagram of tunable anomalous valley Hall effect in hole doped ML GdI $_2$ at the K and K' valley, respectively. The holes are denoted by red “+” symbol. Upward arrows in light blue color and downward arrows in light brown color refer to the spin-up and spin-down carriers, respectively.

and d_{xy} orbitals are degenerate and hybridize with d_{z^2} orbital. Similar orbital distribution is also found in 2D 2H-MoS $_2$ [57]. Without magnetic exchange interaction, SOC still induces spin nondegeneracy at both K and K' valley from the absence of spatial inversion symmetry, but two valleys are energetically degenerate with opposite spins due to the time reversal symmetry, like 2D TMDs [17]. Therefore, the relatively strong SOC effect combined with the magnetic exchange interaction of Gd- d electrons make the significant spontaneous valley polarization in ML GdI $_2$.

C. Valley Hall effect in ML GdI $_2$

Berry curvature $\Omega(k)$ is a powerful tool to study the Hall effect. It is known that in hexagonal systems with broken space inversion symmetry, the charge carriers in the K and K' valleys will acquire a nonzero Berry curvature along the out of plane direction (z direction). When the time reversal symmetry is also broken, the valley contrasting feature will be produced. To confirm this, the Berry curvature of ML GdI $_2$ is calculated based on the Kubo formula [58], which can be written as a summation of all occupied bands contributions:

$$\Omega(k) = - \sum_n \sum_{n' \neq n} f(n) \frac{2\text{Im}\langle \varphi_{nk} | v_x | \varphi_{n'k} \rangle \langle \varphi_{n'k} | v_y | \varphi_{nk} \rangle}{(E_n - E_{n'})^2}, \quad (1)$$

where n and n' are the band indexes, and $f(n)$, $v_{x(y)}$, φ_{nk} and $\varphi_{n'k}$ are the Fermi-Dirac distribution function for the n th band at a k point, the velocity operator of the Dirac electrons along the x/y direction, and the periodic part of the Bloch wave function with eigenvalue E_n and $E_{n'}$, respectively. The distribution of the calculated Berry curvature of ML GdI $_2$ in the

Brillouin zone and along the high symmetry path are shown in Figs. 3(a) and 3(b), respectively. The Berry curvatures of two valleys are sizable and in opposite signs, but their absolute values are no longer identical around the K and K' points, revealing the typical valley contrasting characteristic in ML GdI $_2$.

With a nonzero out-of-plane Berry curvature, the Bloch electrons in ML GdI $_2$ acquire an anomalous Hall velocity v_{\perp} under an in-plane longitudinal electric field E , in which $v_{\perp} \sim E \times \Omega(k)$ [59]. Quantitatively, the anomalous valley Hall conductivity σ_{xy} , which depends on the position of the Fermi level, can be obtained by integrating the Berry curvature over the Brillouin zone,

$$\sigma_{xy} = \frac{e^2}{\hbar} \int_{BZ} \frac{d^2k}{(2\pi)^2} f(k) \Omega(k). \quad (2)$$

Where $f(k)$ is the Fermi Dirac distribution function.

As shown in Fig. 3(c), when the Fermi level lies between the energies of the valence band at the K and K' valleys, as denoted with two vertical dashed lines (cyan region), a fully spin- and valley-polarized Hall conductivity is generated.

The anomalous valley Hall effect of monolayer GdI $_2$ is illustrated in Fig. 3(d). With proper hole doping, the ML GdI $_2$ is magnetized upward and the spin-up holes from K valley flow to the left side of the sample under an external electric field as shown in the upper schematic of Fig. 3(d). The accumulated holes on the boundary generate a charge Hall current that can be detected by a positive voltage. The band structures of ML GdI $_2$ with holes doping are displayed in Fig. S9 of the SM [45], and the Fermi level is shifted down into the valley splitting gap between K and K' points.

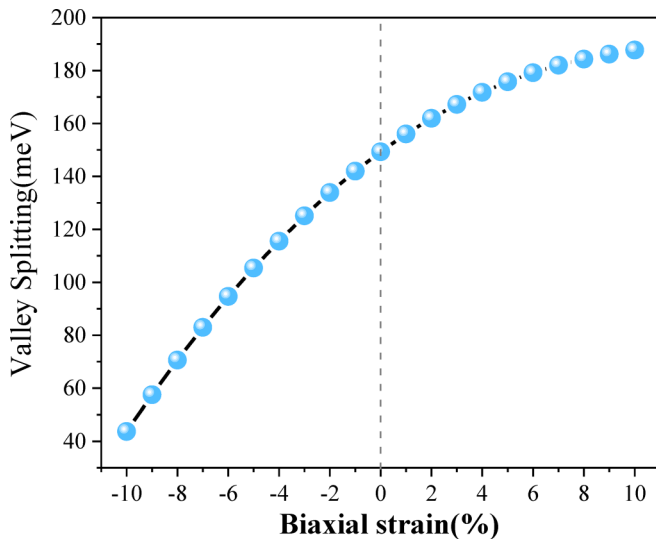


FIG. 4. Variation of valley splitting of ML GdI₂ as a function of in-plane biaxial strains from -10% to 10% .

On the contrary, when the GdI₂ is magnetized downward, the spin-down holes from K' valley transfer to the right edge of the sample due to the opposite Berry curvature, and a negative voltage can be measured [see the lower panel of Fig. 3(d)]. Because of the negligible Berry curvature at the center of Brillouin zone, the carriers in the Γ valley will pass through the ribbon directly without transverse deflection. Accordingly, the valley pseudospin can be selectively manipulated in ML GdI₂ ferrovalley material and read out by electric measurement. Such a property forms the basis for the application of the valleytronics, such as data process or data storage.

D. Effects of strain on valley splitting

In device fabrication, a 2D material is often supported by a substrate which is likely to introduce strain to a 2D material due to lattice mismatch. A biaxial in-plane strain is theoretically applied on ML GdI₂ to study the robustness of the ferrovalley feature against the strain effects. The magnitude of the strain is defined by $\varepsilon = (a - a_0)/a_0$, where a and a_0 represent the in-plane lattice constants of ML GdI₂ with and without strain, respectively. Calculations are performed for the biaxial in-plane strain in the range of -10% to 10% , in which the negative and positive percentage refer to the compressive and tensile strain, respectively. As shown in Fig. 4, the valley splitting increases monotonically with the increase

of biaxial tensile strain. And a giant valley splitting gap of about 189 meV is obtained at 10% tensile strain. Similar behavior has also been reported in MoTe₂ monolayer on the top of EuO(111) substrate [12] and multiferroic CuCrP₂Te₆ monolayer [60]. Conversely, a compressive strain decreases the valley splitting, but the valley splitting gap remains significant (over 40 meV) under a large compressive strain of 10%, which implies that the valley polarization is robust against the biaxial strains. For a potential valley polarized material, a large valley splitting gap is necessary to readily access and manipulate valleys for memory and logic applications. Therefore, the ML GdI₂ is an excellent ferrovalley material in which the nonvolatile anomalous valley Hall effect would be produced, and it can be easily controlled by flipping the magnetization direction of system through a moderate external magnetic field.

IV. CONCLUSION

In sum, by first principles calculations, we reveal that ML GdI₂ can be mechanically exfoliated and it possesses excellent structural thermal dynamic stability. Interestingly, it is an extraordinary intrinsic ferrovalley material with a giant valley splitting gap up to 149 meV, which is large enough for room temperature operation for valleytronic application. This fascinating feature arises from the joint effects of d orbital magnetic exchange interaction and strong spin orbital coupling effect of Gd atom. And the valley contrasting Berry curvature in ML GdI₂ offers an opportunity to selectively manipulate the valley states, and control the anomalous valley Hall effect. Besides, the biaxial tensile strains will further enhance the valley splitting gap up to 189 meV when the strain reaches to $+10\%$. On the contrary, the compressive strains decrease the valley splitting gap, but the valley feature is still preserved even for applying -10% strain, indicating that the valley polarization of ML GdI₂ is robust against the external strains. Overall, ML GdI₂ is a promising ferrovalley material for valleytronic applications.

ACKNOWLEDGMENTS

This research is supported by the Ministry of Education, Singapore, under its MOE AcRF Tier 2 Award No. MOE2019-T2-2-030 and MOE AcRF Tier 1 Awards No. R-144-000-441-114 and No. R-144-000-413-114. The authors thank Dr. L. Xu for his helpful discussion and suggestions. We acknowledge the National Supercomputing Centre Singapore for computational resources.

- [1] L. J. Sham, S. J. Allen, A. Kamgar, and D. C. Tsui, *Phys. Rev. Lett.* **40**, 472 (1978).
- [2] S. A. Wolf, D. D. Awschalom, R. A. Buhrman, J. M. Daughton, S. von Molnár, M. L. Roukes, A. Y. Chtchelkanova, and D. M. Treger, *Science* **294**, 1488 (2001).
- [3] K. F. Mak, D. Xiao, and J. Shan, *Nat. Photon.* **12**, 451 (2018).
- [4] A. Rycerz, J. Tworzydło, and C. W. J. Beenakker, *Nat. Phys.* **3**, 172 (2007).
- [5] X. Xu, W. Yao, D. Xiao, and T. F. Heinz, *Nat. Phys.* **10**, 343 (2014).
- [6] H. Zeng, J. Dai, W. Yao, D. Xiao, and X. Cui, *Nat. Nanotechnol.* **7**, 490 (2012).
- [7] K. F. Mak, K. L. McGill, J. Park, and P. L. McEuen, *Science* **344**, 1489 (2014).
- [8] G. Aivazian *et al.* *Nat. Phys.* **11**, 148 (2015).
- [9] D. MacNeill, C. Heikes, K. F. Mak, Z. Anderson, A. Kormányos, V. Zólyomi, J. Park, and D. C. Ralph, *Phys. Rev. Lett.* **114**, 037401 (2015).
- [10] Y. C. Cheng, Q. Y. Zhang, and U. Schwingenschlögl, *Phys. Rev. B* **89**, 155429 (2014).

- [11] N. Singh and U. Schwingenschlöggl, *Adv. Mater.* **29**, 1600970 (2017).
- [12] Q. Zhang, S. A. Yang, W. Mi, Y. Cheng, and U. Schwingenschlöggl, *Adv. Mater.* **28**, 959 (2016).
- [13] L. Xu, M. Yang, L. Shen, J. Zhou, T. Zhu, and Y. P. Feng, *Phys. Rev. B* **97**, 041405(R) (2018).
- [14] H. Zhang, W. Yang, Y. Ning, and X. Xu, *Phys. Rev. B* **101**, 205404 (2020).
- [15] D. Zhong *et al.*, *Sci. Adv.* **3**, e1603113 (2017).
- [16] T. Hu, G. Zhao, H. Gao, Y. Wu, J. Hong, A. Stroppa, and W. Ren, *Phys. Rev. B* **101**, 125401 (2020).
- [17] W.-Y. Tong, S.-J. Gong, X. Wan, and C.-G. Duan, *Nat. Commun.* **7**, 13612 (2016).
- [18] Z. Song, X. Sun, J. Zheng, F. Pan, Y. Hou, M.-H. Yung, J. Yang, and J. Lu, *Nanoscale* **10**, 13986 (2018).
- [19] J. Zhou, Y. P. Feng, and L. Shen, *Phys. Rev. B* **102**, 180407(R) (2020).
- [20] P. Zhao, Y. Ma, C. Lei, H. Wang, B. Huang, and Y. Dai, *Appl. Phys. Lett.* **115**, 261605 (2019).
- [21] Y. Zang, Y. Ma, R. Peng, H. Wang, B. Huang, and Y. Dai, *Nano Res.* **14**, 834 (2021).
- [22] R. Peng, Y. Ma, X. Xu, Z. He, B. Huang, and Y. Dai, *Phys. Rev. B* **102**, 035412 (2020).
- [23] W. Du, Y. Ma, R. Peng, H. Wang, B. Huang, and Y. Dai, *J. Mater. Chem. C* **8**, 13220 (2020).
- [24] B. Wang, X. Zhang, Y. Zhang, S. Yuan, Y. Guo, S. Dong, and J. Wang, *Mater. Horiz.* **7**, 1623 (2020).
- [25] G. Kresse and D. Joubert, *Phys. Rev. B* **59**, 1758 (1999).
- [26] P. E. Blöchl, *Phys. Rev. B* **50**, 17953 (1994).
- [27] G. Kresse and J. Furthmüller, *Phys. Rev. B* **54**, 11169 (1996).
- [28] G. Kresse and J. Furthmüller, *Comput. Mater. Sci.* **6**, 15 (1996).
- [29] J. P. Perdew, K. Burke, and M. Ernzerhof, *Phys. Rev. Lett.* **80**, 891 (1998).
- [30] J. P. Perdew, K. Burke, and M. Ernzerhof, *Phys. Rev. Lett.* **77**, 3865 (1996).
- [31] S. Grimme, *J. Comput. Chem.* **27**, 1787 (2006).
- [32] S. L. Dudarev, G. A. Botton, S. Y. Savrasov, C. J. Humphreys, and A. P. Sutton, *Phys. Rev. B* **57**, 1505 (1998).
- [33] G. Xu, J. Wang, C. Felser, X.-L. Qi, and S.-C. Zhang, *Nano Lett.* **15**, 2019 (2015).
- [34] S. Steiner, S. Khmelevskiy, M. Marsmann, and G. Kresse, *Phys. Rev. B* **93**, 224425 (2016).
- [35] A. Togo and I. Tanaka, *Scr. Mater.* **108**, 1 (2015).
- [36] X. Gonze and C. Lee, *Phys. Rev. B* **55**, 10355 (1997).
- [37] D. Bucher, L. C. T. Pierce, J. A. McCammon, and P. R. L. Markwick, *J. Chem. Theory Comput.* **7**, 890 (2011).
- [38] S. Nosé, *Mol. Phys.* **52**, 255 (1984).
- [39] S. Nosé, *J. Chem. Phys.* **81**, 511 (1984).
- [40] A. A. Mostofi, J. R. Yates, Y.-S. Lee, I. Souza, D. Vanderbilt, and N. Marzari, *Comput. Phys. Commun.* **178**, 685 (2008).
- [41] A. Kasten, P. H. Müller, and M. Schienle, *Solid State Commun.* **51**, 919 (1984).
- [42] C. Felser, K. Ahn, R. K. Kremer, R. Seshadri, and A. Simon, *J. Solid State Chem.* **147**, 19 (1999).
- [43] K. Ahn, C. Felser, R. Seshadri, R. K. Kremer, and A. Simon, *J. Alloys Compd.* **303**, 252 (2000).
- [44] J. Deisenhofer, H. A. Krug von Nidda, A. Loidl, K. Ahn, R. K. Kremer, and A. Simon, *Phys. Rev. B* **69**, 104407 (2004).
- [45] See Supplemental Material at <http://link.aps.org/supplemental/10.1103/PhysRevB.103.125121> for more simulation results on the structural, mechanical, and electronic properties of ML and bulk GdI₂, which includes Refs. [19,46–54].
- [46] R. Zacharia, H. Ulbricht, and T. Hertel, *Phys. Rev. B* **69**, 155406 (2004).
- [47] R. Andrew, R. Mapasha, A. Ukpong, and N. Chetty, *Phys. Rev. B* **85**, 125428(2012).
- [48] T. J. Booth *et al.*, *Nano Lett.* **8**, 2442 (2008).
- [49] A. Jain *et al.*, *APL Mater.* **1**, 011002 (2013).
- [50] X. Li, X. Wu, Z. Li, J. Yang, and J. G. Hou, *Nanoscale* **4**, 5680 (2012).
- [51] H. Cheng, J. Zhou, M. Yang, L. Shen, J. Linghu, Q. Wu, P. Qian, and Y. P. Feng, *J. Mater. Chem. C* **6**, 8435 (2018).
- [52] Q. Pei, X. Wang, J. Zou, and W. Mi, *J. Mater. Chem. C* **6**, 8092 (2018).
- [53] N. Luo, C. Si, and W. Duan, *Phys. Rev. B* **95**, 205432 (2017).
- [54] L. Yuan, Z. Li, and J. Yang, *Phys. Chem. Chem. Phys.* **15**, 497 (2013).
- [55] S. A. Vitale, D. Nezich, J. O. Varghese, P. Kim, N. Gedik, P. Jarillo-Herrero, D. Xiao, and M. Rothschild, *Small* **14**, 1801483 (2018).
- [56] T. Norden, C. Zhao, P. Zhang, R. Sabirianov, A. Petrou, and H. Zeng, *Nat. Commun.* **10**, 4163 (2019).
- [57] G.-B. Liu, D. Xiao, Y. Yao, X. Xu, and W. Yao, *Chem. Soc. Rev.* **44**, 2643 (2015).
- [58] D. J. Thouless, M. Kohmoto, M. P. Nightingale, and M. den Nijs, *Phys. Rev. Lett.* **49**, 405 (1982).
- [59] D. Xiao, M.-C. Chang, and Q. Niu, *Rev. Mod. Phys.* **82**, 1959 (2010).
- [60] X. Ma, L. Sun, J. Liu, X. Feng, W. Li, J. Hu, and M. Zhao, *Phys. Status Solidi (RRL)* **14**, 2000008 (2020).